PHYSICAL REVIEW FLUIDS **2**, 044003 (2017)

Hydrodynamic waves in films flowing under an inclined plane

Wilko Rohlfs* and Philipp Pischke
Institute of Heat and Mass Transfer, RWTH Aachen University, Augustinerbach 6, 52056 Aachen, Germany

Benoit Scheid†
TIPs Laboratory, Université Libre de Bruxelles, Code Postal 165/67, Avenue Franklin Roosevelt 50, 1050 Bruxelles, Belgium

(Received 29 February 2016; published 7 April 2017)

This study addresses the fluid dynamics of two-dimensional falling films flowing underneath an inclined plane using the weighted integral boundary layer (WIBL) model and direct numerical simulations (DNSs). Film flows under an inclined plane are subject to hydrodynamic and Rayleigh-Taylor instabilities, leading to the formation of two- and three-dimensional waves, rivulets, and eventually dripping. The latter can only occur in film flows underneath an inclined plane such that the gravitational force acts in a destabilizing manner by pulling liquid into the gaseous atmosphere. The DNSs are performed using the solver interFoam of the open-source code OpenFOAM with a gradient limiter approach that avoids artificial oversharpening of the interface. We find good agreement between the two model approaches for wave amplitude and wave speed irrespectively of the orientation of the gravitational force and before the onset of dripping. The latter cannot be modeled with the WIBL model by nature as it is a single-value model. However, for large-amplitude solitarylike waves, the WIBL model fails to predict the velocity field within the wave, which is confirmed by a balance of viscous dissipation and the change in potential energy. In the wavy film flows, different flow features can occur such as circulating waves, i.e., circulating eddies in the main wave hump, or flow reversal, i.e., rotating vortices in the capillary minima of the wave. A phase diagram for all flow features is presented based on results of the WIBL model. Regarding the transition to circulating waves, we show that a critical ratio between the maximum and substrate film thickness (approximately 2.5) is also universal for film flows underneath inclined planes (independent of wavelength, inclination, viscous dissipation, and Reynolds number).

DOI: 10.1103/PhysRevFluids.2.044003

I. INTRODUCTION

Falling liquid films are gravity-driven free-surface flows subject to various instabilities leading to a deformed and wavy interface. Owing to their use in different applications in process and energy engineering, they are widely studied (see [1] for a review). In contrast to classical films flowing down the top side of inclined plates, this study examines films flowing down the bottom side, as shown in Fig. 1 (right plot). This type of flow has also been called negative gravity [2], in association with the negative value of the inclination number (defined later), where the gravitational body force destabilizes the film flow. As illustrated in Fig. 1 for the stabilizing gravity case, the crosswise component of gravity g_y is pointing towards the wall (the negative y coordinate); it is the opposite for the case of destabilizing gravity. Film flows on the upper and lower sides of inclined walls exist in many types of fills, which are used in cooling towers. Those fillings are complex structures often made from Polyvinyl Dichloride to create a high surface area of the film flow, long resident times, and a minimum air-side pressure drop. While waves induced by the inherent hydrodynamic instability

*rohlfs@wsa.rwth-aachen.de
†bscheid@ulb.ac.be

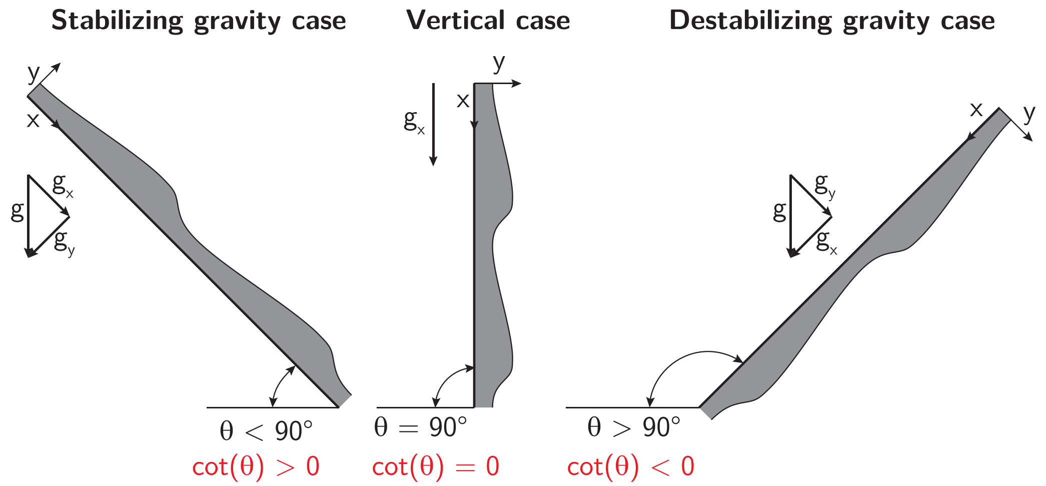

FIG. 1. Schematic and definition of falling film flows under stabilizing and destabilizing gravity conditions.

increase the surface area, dripping of the liquid reduces the residence time. As such, information about wave regimes for film flows on the upper and lower sides of the substrate as well as dripping limits would support the design of effective fills.

Compared to vertical or inclined falling films, only a small number of research studies exist for films flowing down the underside of an inclined plate. In the work of Oron and Rosenau [2] the temporal evolution of a film on a horizontal and inclined ceiling is shown. While for the horizontal case [see also the Rayleigh-Taylor (RT) instability below] waves with infinite surface gradients are formed, a tilted ceiling results in the formation of high-amplitude traveling waves. A combined experimental and numerical study on droplet detachment using a permeable wall was conducted by Abdalall *et al.* [3]. Different injection rates were investigated for a horizontal and an inclined surface (with an inclination angle of 2.5°). The main findings of their study include that droplets detaching from horizontal surfaces have larger equivalent diameter than those pinching off from an inclined plane. From this observation, the authors conclude that the mean liquid film thickness is smaller for the inclined plane than for a horizontal plane. However, the authors do not question whether the formation of droplet detachment can be suppressed by an inclined surface.

In the remainder of this introduction, we define the problem and the associated parameters, discuss the limiting case of a horizontal film subjected to RT instability, and present the different flow features encountered in falling films.

A. Definition of the film flow and the dimensionless parameters

The dominant forces of falling films on the upper or lower sides of an inclined plane (as illustrated in Fig. 1) include the gravitational body force, shear-driven viscous forces, and surface tension forces on the phase boundary. While inertia destabilizes, surface tension stabilizes the flow. The crosswise component of gravity g_y stabilizes the flow on the upper side of an inclined plane but destabilizes the flow on the lower side. The main characteristic from the physical perspective is the boundary-layer-type flow in which the scale of streamwise variations is much smaller than the scale of crosswise variations.

From the set of dominant forces, a set of dimensionless parameters arise that characterizes the film flow. These parameters are the film-thickness-based Reynolds number Re_{h_N}, Kapitza number Γ, and inclination number $\mathcal{C}$:

$$\mathrm{Re}_{h_N} = \frac{g \sin\theta h_N^3}{3\nu^2}, \quad \Gamma = \frac{\sigma}{\rho \nu^{4/3}(g \sin\theta)^{1/3}}, \quad \mathcal{C} = \cot\theta. \tag{1}$$

Alternatively, the perpendicular Kapitza number $\Gamma_\perp = \Gamma(\sin\theta)^{1/3}$ can be used, which is constant for a given fluid. The symbol g describes the gravitational acceleration, h_N the film thickness of the Nusselt flat-film solution, ρ the density, ν the kinematic viscosity, σ the surface tension, and θ the inclination angle. Since the cotangent of $\theta > 90^\circ$ yields a negative value, the film flow underneath an inclined plane is also called negative gravity. One can also define the flow-rate-based Reynolds number $\mathrm{Re}_{q_N} = q_N/\nu$, where q_N is the width-specific volume flow rate at the inlet. Only for the flat film $\mathrm{Re}_{q_N} = \mathrm{Re}_{h_N}$ holds.

Another set of scaling parameters, named Shkadov scaling, is given by

$$\delta = \frac{(3\,\mathrm{Re})^{11/9}}{\Gamma^{1/3}}, \quad \zeta = \frac{\mathcal{C}(3\,\mathrm{Re})^{2/9}}{\Gamma^{1/3}}, \quad \eta = \frac{(3\,\mathrm{Re})^{4/9}}{\Gamma^{2/3}}, \tag{2}$$

with δ the reduced Reynolds number, ζ the reduced inclination number, and η the extensional viscous number associated with extensional viscous stresses. This scaling accounts for the balance of gravity and viscous drag with surface tension, which is relevant for large-amplitude waves [1] and gathers all second-order viscous effects in the boundary layer equations in front of the parameter η. For a vertical wall ($\zeta = 0$) and negligible extensional viscous effects ($\eta = 0$), the Shkadov scaling reduces to a single parameter δ, describing all effects of small- or large-amplitude solitary waves [1].

B. Rayleigh-Taylor instability and saturation mechanisms in a horizontal film

The limiting case of a horizontal film with destabilizing gravity corresponds to the well-known case of the Rayleigh-Taylor instability with a denser fluid resting initially on top of a less dense fluid. The entire system is described by a balance of gravitational and surface tension forces. While the gravitational force acts in a destabilizing way, the surface tension stabilizes.

For an infinite domain, the flow configuration is unstable with respect to infinitesimal disturbances, as shown in the classical paper of Rayleigh [4]. A comprehensive description of the instability is given in the work of Chandrasekhar [5] and a combined experimental and theoretical study revealing insights into the pattern formation is given by Fermigier *et al.* [6]. In the case of a finite domain, a critical wavelength exists below which the flow configuration is stable. According to the linear stability analysis, this wavelength is given by

$$\lambda_{c,\mathrm{RT}} = 2\pi\left(\frac{\sigma}{(\rho_l - \rho_g)g}\right)^{1/2}, \tag{3}$$

where σ is the surface tension, ρ_l is the liquid density, ρ_g is the gas density, and g is the gravity. For the stagnant flow configuration of the Rayleigh-Taylor instability, the long-wave perturbations of small amplitudes grow exponentially in the beginning before nonlinear effects become important. Due to the absence of any saturation, the perturbations increase up to the formation of a detaching droplets, hereafter referred to as dripping.

Fermigier *et al.* [6] discuss the existence of a threshold for dripping that is related to a critical volume of fluid for the stability of a hanging drop. This critical volume is known from the work of Myshkis *et al.* [7]. The volume of liquid accumulated in a single hanging droplet can be approximated by the initial film thickness and the area of a hexagon with lateral expansions given by the critical wavelength. If this volume exceeds the critical one, Fermigier *et al.* state that initial disturbances grow up to the point of dripping. If the volume is lower than the critical one, this film is in the first stage stable, but dripping occurs unavoidably after droplet coalescence.

Saturation of the Rayleigh-Taylor instability and consequently a suppression of dripping can be achieved in different ways, such as applying oscillations [8], an electric field, or temperature gradients [9–11]. In addition, curvature can suppress the Rayleigh-Taylor instability as shown in the theoretical and experimental work of Trinh *et al.* [12]. The drainage behavior of a thin liquid film in a horizontal cylinder is investigated, showing that initial surface deformations decrease or increase depending on the ratio between gravitational and surface tension forces (ratio between initial film thickness and cylinder radius for fixed fluid properties). A saturation mechanism in close relation

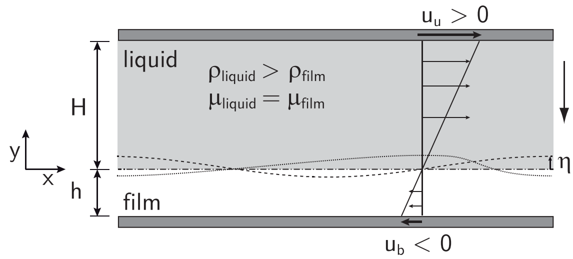

FIG. 2. Configuration of the Rayleigh-Taylor instability in a Couette-type flow (drawing according to the description of [13]). The dash-dotted line represents the undisturbed interface, the dashed line shows a sinusoidal deformation, and the dotted line illustrates the interface deformed due to advection.

to falling films has been demonstrated by Babchin *et al.* [13], showing that an advective flow in the horizontal direction, due to a plate moving at constant velocity as in a Couette flow, can lead to saturation of the Rayleigh-Taylor instability.

Figure 2 illustrates the flow configuration of two incompressible liquids with equal viscosities. The thickness of the lower fluid layer (film) is assumed to be much thinner and less dense than the upper liquid layer. The upper plate moves in the x direction at constant velocity U_u and the bottom plate moves in the negative-x direction at a velocity U_b such that the unperturbed fluid layer at the interface is at rest. The time-dependent profile of the surface deformation is described by the variable $\eta(t,x)$. Assuming a symmetric (sinusoidal) deformation, as illustrated by the dashed line in Fig. 2, each point of the interface moves in the horizontal direction with the velocity proportional to the elevation η. This symmetric deformation is not sustained since positive deformations ($\eta > 0$) move in the positive-x direction while negative deformations ($\eta < 0$) move in the opposite direction. As a result, the deformation (wave) profile steepens, thus increasing the curvature of the surface (dotted line in Fig. 2). An eventual breakup is prevented by surface tension, which becomes important when the steepening process has advanced sufficiently. Thus, surface tension reduces excessive elevations of the interface. The balance of the three mechanisms, destabilizing gravity, flow-induced steepening of the surface profile, and stabilizing surface tension, results in a saturated and stable interface of the finite-amplitude perturbation.

Besides the saturation behavior of instabilities, another main characteristic is the distinction between convective and absolute instability. Brun *et al.* [14] recently demonstrated in the limit of negligible inertia and viscous extensional stress the existence of a critical (fluid and flow specific) angle at which the Rayleigh-Taylor instability is convectively transported, e.g., the instability changes from absolute to convective type. Using the weighted integral boundary layer model, an extension to larger-Reynolds-number flows is presented by Scheid *et al.* [15]. A strong dependence on the vertical Kapitza number and a significant effect of viscous extensional stress have been identified. While for low values of the Reynolds number surface tension is the main stabilizing mechanism, the convective transport dominates the convective or absolute instability for high-Reynolds-number flows.

C. Criteria for phase transitions

In a previous paper [16], two-dimensional film flows on the top side of an inclined plate have been examined using DNS and the weighted residual integral boundary layer (WIBL) model. An analytical criterion for the onset of circulating waves has been determined from the WIBL model based on the wave celerity, the average film thickness, and the maximum film thickness as summarized in Table I and outlined in Appendix B. For the onset of flow reversal, a similar criterion using instead the minimum film thickness was provided. Furthermore, phase diagrams for the two transitions have been drawn, clearly separating the different wave features.

TABLE I. Criteria for the onset of circulating waves and flow reversal. Note that the criteria in terms of wave celerity c are based on a semiparabolic velocity profile neglecting first-order corrections. All criteria depend on either the average film thickness $\langle h \rangle_\lambda$ or the average flow rate $\langle q \rangle_\lambda$ and on the maximum or minimum film thickness. A detailed derivation of the criteria is given in Ref. [16] and in Appendix B, while definitions of closed and open flow conditions are given in Appendix A.

Onset of	Closed flow	Open flow
circulating waves	$c_{\mathrm{circ}} = \frac{1}{3\langle h \rangle_\lambda - h_{\max}}$	$c_{\mathrm{circ}} = \frac{3\langle q \rangle_\lambda}{3 - h_{\max}}$
flow reversal	$c_{\mathrm{rev}} = \frac{1}{3(\langle h \rangle_\lambda - h_{\min})}$	$c_{\mathrm{rev}} = \frac{\langle q \rangle_\lambda}{1 - h_{\min}}$

In a recent study by Reck and Aksel [17], recirculation zones underneath solitary waves were studied experimentally. Contrary to our statement that the critical parameter for the onset of circulating waves only depends on the ratio between the maximum and substrate film thickness, Reck and Aksel conclude an additional dependence of this critical ratio from Reynolds number. The main cause for this difference is given by the fact that in the work of Rohlfs and Scheid [16] stationary traveling waves were studied, whereas the solitary waves studied by Reck and Aksel strongly depend on the perturbation amplitude applied at the inlet of the test section. Thus, different wave amplitudes have been observed for the same set of dimensionless parameters (Reynolds number, Kapitza number, and excitation frequency) as demonstrated in Fig. 9 of [17].

The remainder of this paper is structured as follows. Section II provides a comprehensive description of the methods applied. Section III presents the results for the transition between convective and absolute instability, the flow structures of films on the underside of inclined plates, and finally phase diagrams and correlations for the onset of circulating waves and flow reversal for film flows with stabilizing and destabilizing plate inclination. Section IV summarizes.

II. METHODS

In this study the method of fully resolved numerical simulations [direct numerical simulations (DNSs)] and the weighted residual integral boundary layer method (full second-order WIBL model) are applied in the two-dimensional domain. For the DNSs, an approach for interface compression based on a gradient limiter is applied. This compression scheme leads to much better agreement between DNSs and the WIBL model as compared to our previous results presented in Ref. [16].

A. Direct numerical simulation technique

The direct numerical simulations are conducted with the open field operation and manipulation library (OpenFOAM) (see [18–20]) and the interFoam solver, a finite-volume implementation of the volume-of-fluid method [21]. It describes multifluid flows by the cell-average volume fractions of the secondary phase. The free-surface flow of two immiscible and incompressible fluids is numerically calculated by solving the advection of the volume fractions and the fully resolved Navier-Stokes equations for mass and momentum.

As the finite-volume discretization defines cell-average volume fractions, the interface is represented by mixed cells that contain both fluids. To avoid numerical diffusion of the interface, interFoam introduces an artificial antidiffusive flux in the direction normal to the interface, known as the interface compression method. In capillary-dominated flows as considered here, interfacial forces must be obtained from the curvature of the interface. If the exact interface location is not required, interface curvature can be reconstructed from the divergence of the interface normal vector using vector field calculus, which is implemented in the interFoam solver. The resulting interfacial forces are converted into cell-average volume forces by the continuum surface force method [22].

Due to accuracy limitations in interFoam [23], the interface compression scheme was amended by a limiter to avoid artificial oversharpening of the interface and interfacial forces are calculated by the continuum surface stress method [24]. This variant of interFoam has the following advantages over its original. First, capillary pressures are predicted correctly. Second, predictions do not depend on the strength of the antidiffusive flux. Third, the predictions are independent of the frame of reference, which is not the case with the original interFoam formulation, but crucial to calculations of traveling waves in falling liquid films, which can be considered steady-state problems in a frame of reference moving at phase velocity. A detailed description of the model together with a validation based on various test cases (capillary wave, droplet, etc.) is given in Ref. [25] and validation for the case of falling liquid films is provided in Sec. III.

B. Weighted residual integral boundary layer method

The weighted residual method, which was derived by Ruyer-Quil and Manneville [26] for modeling falling liquid films, reduces the system of two-dimensional conservation equations (for mass and momentum) and the boundary conditions at the wall and at the free surface to a model of evolution equations for the local film thickness h and the streamwise flow rate q. To reduce the set of equations, the streamwise velocity field is projected onto a set of polynomials. The Galerkin method is used to substitute these projections into the integrated conservation equations.

In the full second-order WIBL model (WIBL2), which is given in Appendix A [Eqs. (A1)–(A9)], additional evolution equations correct the flow rate by accounting for the deviations from the parabolic velocity profile due to second-order inertia effects. A further reduction of the system of equations is obtained in the moving frame of reference for stationary periodic traveling waves. In this case, the equations reduce to a fifth-order dynamical system of ordinary differential equations. An explicit formulation for the highest derivatives [h_{xxx} in Eq. (A7)] results in a quotient that gives a limitation to the denominator that is required to be nonzero, introducing the condition

$$\frac{hc}{q_0} > -\frac{76}{11} \pm \frac{2\sqrt{2665}}{11} \approx 2.477\text{–}16.295, \tag{4}$$

where h is the local film thickness, c is the wave celerity, and q_0 is the volume flow rate at (per unit length in the spanwise direction) which the fluid moves under the wave. Keeping in mind that $q_0 < 0$, condition (4) can be interpreted as a limit on the maximum wave amplitude that can be calculated using the dynamical system approach. For film flows on the upper side of inclined planes (gravity stabilizes the film), this condition does not limit the models applicability because the amplitude of the waves is not sufficiently large. However, for destabilizing gravity cases, this condition has been found to limit the models applicability. Note that this is not a general limitation of the WIBL2 model and that waves of higher amplitude can be obtained using the time-dependent version of the model. The equations of the dynamical system can be solved by using the continuation and bifurcation tool for ordinary differential equations in the software AUTO-07P [27] and the package HOMCONT for homoclinic solutions.

III. RESULTS

In Sec. III A a direct comparison of WIBL2 and DNS results with experimental data is provided for two different sets of parameters. These sets are also the starting point for the investigation of films on the underside of an inclined plane. A more general view on wave amplitude and wave speed is provided in Sec. III B, in which homoclinic solutions are also investigated using WIBL2. Furthermore, a phase diagram for the onset of circulating waves and flow reversal is presented. Section III C addresses these phase transitions in the limit cycle (depending on wave frequency).

A. Particular cases of films on the underside of inclined plates

In this section the behavior of falling films on the underside of an inclined plate will be examined for two specific wave patterns, for which experimental validation data are available for the vertical case [28]. Unfortunately, no sufficient experimental data are available for hanging films that are

TABLE II. Parameters used in the simulations and corresponding to experimental data for a vertical film. The film-thickness-based Reynolds number Re_{h_N} and the wavelength λ_x have been determined iteratively by direct numerical simulations with periodic boundary conditions for which the closed flow condition applies, with the aim of matching the flow-rate-based Reynolds number Re_{q_N} and the frequency f from the experiment, for which in turn the open flow condition applies. Note that the scaling for the wave number k_x corresponds to $1/h_N\kappa$, where $\kappa = 1/\sqrt{\eta}$.

Parameters	Case 1	Case 2
Expt.		
Re_{q_N}	6.8	15
f	24 Hz	16 Hz
DNS		
Re_{h_N}	5.99	10.76
Ka	509.6	509.6
λ_x	7.24 mm	20.5 mm
WIBL2		
δ_{h_N}	4.28	8.747
η	0.057	0.073
k_x	0.897	0.337

suitable for a validation of the methods. Nevertheless, the use of two completely different numerical approaches revealing very similar results serves as a validation for hanging film flows. Table II provides a summary of the dimensional and dimensionless parameters. For an inclination number of zero (vertical plate), case 1 is characterized by a nearly sinusoidal wave with no circulation in the main hump [$\mathrm{Re}_q = 6.8$ and $f = 24$ Hz (see Fig. 3)]. Case 2 is characterized by a solitarylike wave with the presence of a circulation zone [$\mathrm{Re}_q = 15$ and $f = 16$ Hz (see Fig. 4)]. The numbering of the cases follows our previous study [16]. However, a detailed evaluation of case 2 will be presented first, followed by a short description of case 1. The two mentioned figures also present a direct comparison between experimental results, fully resolved numerical simulations, and the WIBL2 model. Very good agreement is given in the wave shape and the velocity profile between the fully resolved simulations and the WIBL2 model. Note that a similar figure using the standard OpenFOAM interFoam solver was presented in Ref. [16], showing less agreement between the two

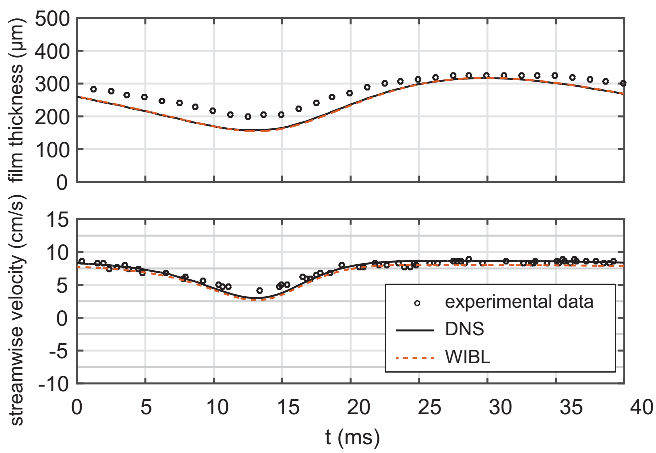

FIG. 3. Comparison of experimental [29] and numerical results for case 1 outlined in Table II, i.e., for $\mathrm{Re}_q = 6.8$. The streamwise velocity is given at 0.1 mm from the plate.

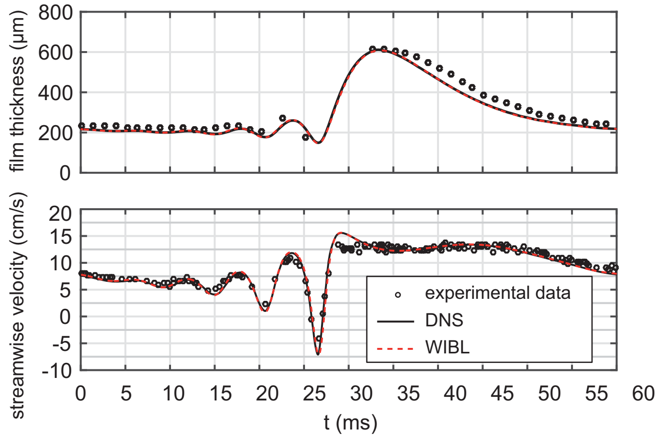

FIG. 4. Same as Fig. 3 for case 2, i.e., $\mathrm{Re}_q = 15$.

approaches. This clearly reveals the importance of precise interface compression and reconstruction methods in DNSs.

Increasing the inclination number (positive values) reveals stabilization of the film flow with a transition of the solitarylike wave (case 2) from a circulating wave to a noncirculating wave [16]. Contrarily, decreasing the inclination number (negative values) destabilizes the flow, as it is associated with an increase of wave amplitude and consequently wave celerity as shown in Fig. 5. While the onset of circulating waves and flow reversal is a transition that can occur for positive inclination numbers as well as for negative inclination numbers, the onset of dripping is strictly associated with destabilizing gravity. Thus, the inclination number for cases 1 and 2 is decreased in the following to the point when dripping occurs in the direct numerical simulations. Practically, the inclination number is decreased by introducing an additional acceleration in the cross-stream direction while keeping the average film thickness, the acceleration in the streamwise direction, and the wavelength constant (δ_{h_N} and η are constant). Note that the present form of dripping in a two-dimensional domain corresponds to the detachment of a ligament with an infinite expansion in the spanwise direction.

1. Case 2: Solitarylike wave

Figure 5 illustrates the velocity field by isolines of the stream function of the falling liquid film for different values of the reduced inclination number ζ towards negative values, as obtained by DNS and the WIBL2 model. The stream function of the results of the WIBL2 model is calculated based on the velocity field given by Eq. (C1) (see Appendix C), including second-order corrections to the leading-order parabolic profile (s_1 and s_2). For positive (not shown; see [16]) and negative inclination numbers down to $\zeta = -1.2$, the two model approaches show excellent agreement in the wave shape and the velocity field (see the top plot in Fig. 5). For the case with $\zeta = -1.2$, the wave is characterized by a large circulation zone visible in the moving frame of reference. Wave amplitude and wave celerity predicted by the two approaches are very similar, as shown in Figs. 6 and 7, respectively. However, decreasing the inclination number further down results in significant differences, especially in the reconstructed velocity field as shown for $\zeta = -1.5$ and $\zeta = -1.9$. In both cases, the velocity field predicted by the WIBL2 model exhibits an unphysical pattern in the main wave hump and clearly reveals that the validity of the boundary layer model is violated.

The significant differences between DNS and the WIBL2 model in the velocity field are further examined to identify the validity range of the model. The artificial velocity field in Fig. 5 for $\zeta = -1.9$ shows two counterrotating vortices that induce high shear and consequently a higher viscous dissipation than the single vortex predicted by DNS. Figure 8 (left plot) presents the

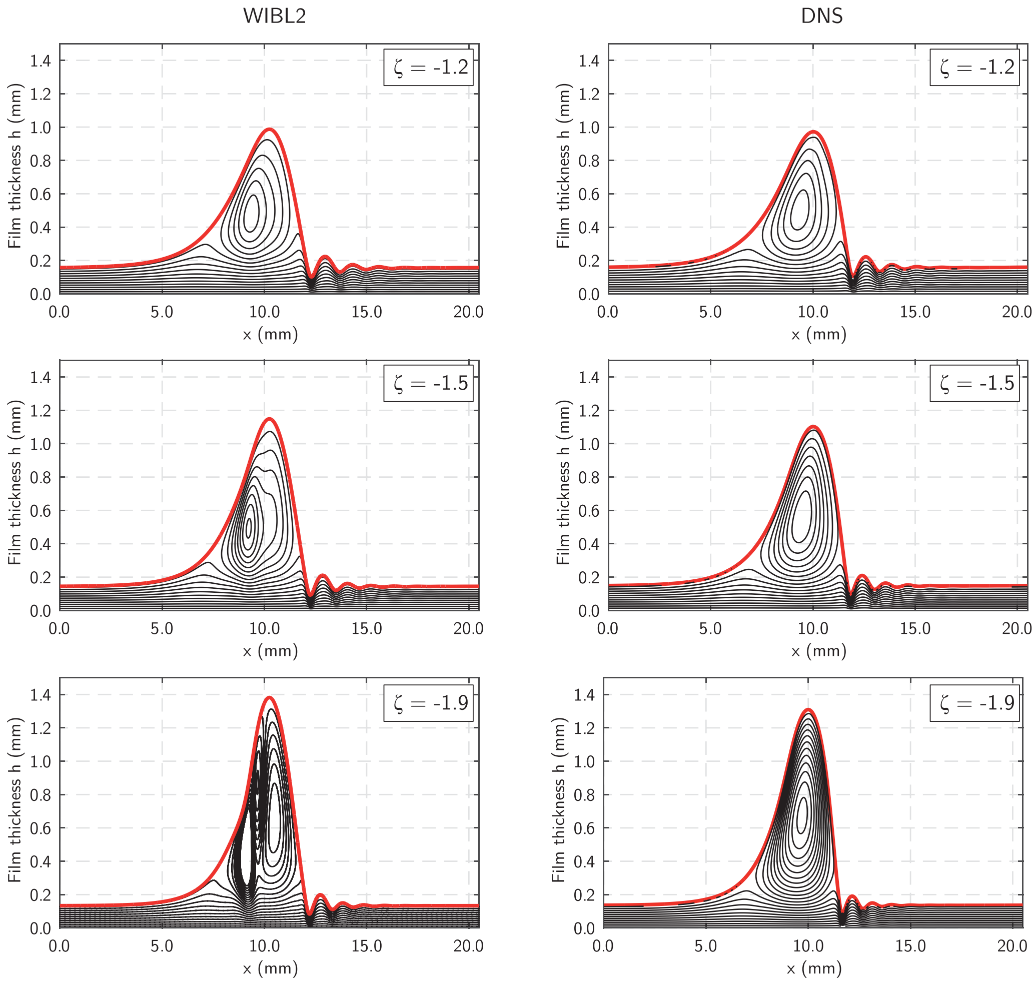

FIG. 5. Inclined film flow for case 2 and $\zeta = [-1.2, -1.5, -1.9]$. Wave profiles and streamlines are shown in a moving frame of reference at velocity c. Contour lines are shown for $\Delta\psi = 5 \times 10^{-6}$ m^2/s.

reconstructed velocity profile for the same flow configuration neglecting the influence of s_1 and s_2 by setting those variables to zero. In this case, there is only one rotating vortex very similar to the results obtained by DNS, which clearly reveals that the corrections are the main cause for the incorrect and artificial velocity profile.

Furthermore, an energy balance based on Eqs. (D4) and (D5) in Appendix D is shown in Fig. 8 (right plot) by presenting the quotient of the dissipation rate and the change in potential energy. In general, these two energies should balance each other such that the quotient takes a value of one, which is confirmed for $\zeta > -1.2$ (accounting for the corrections s_1 and s_2). However, the plot clearly reveals an imbalance for high negative values of ζ, with an overprediction of viscous dissipation. The same quotient has also been calculated for the velocity profile that has been obtained by neglecting the corrections s_1 and s_2. Clearly, there is an underprediction of viscous dissipation for the entire parameter range of ζ. However, for high negative values of ζ, the imbalance does not diverge as compared to the viscous dissipation calculated with the velocity field including s_1 and s_2 corrections.

Despite the model limitations at high-amplitude waves (for high negative-ζ values), remarkably good agreement between DNS and WIBL2 model is given below this limitation. Decreasing the inclination number down to $\zeta = -2$ finally results in dripping of the film flow in the DNS as shown

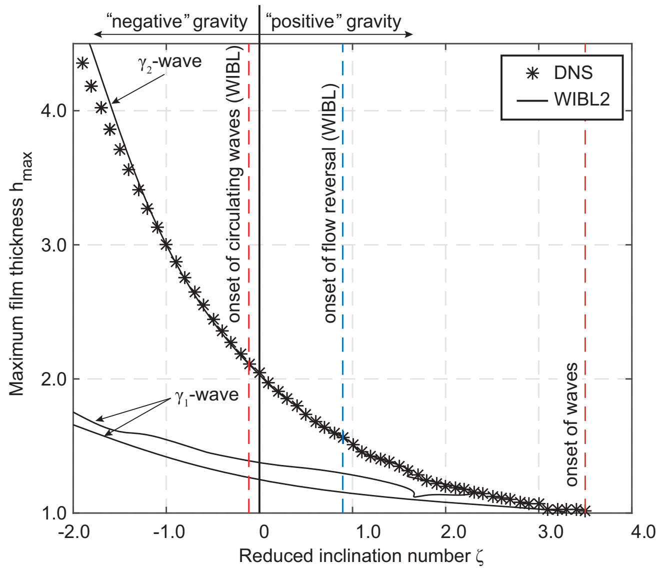

FIG. 6. Influence of stabilizing and destabilizing gravity on the maximum film thickness by varying the inclination number ζ for the flow configuration corresponding to case 2. The closed flow boundary condition is applied for both the DNS and the WIBL2 model. The red line correspondeds to WIBL results including the full curvature formulation.

in Fig. 9 for case 2. This dripping behavior cannot be predicted by the WIBL2 model, which only allows for a unique value of h for each streamwise position.

Figures 6 and 7 show the characteristic values of maximum film thickness and wave celerity, respectively. Note that the branch of solutions obtained with AUTO-07P switches from γ_1 (dip waves) to γ_2 (hump) waves [30] at the turning point $\zeta = 2.28$ and that the γ_2 branch could not be continued

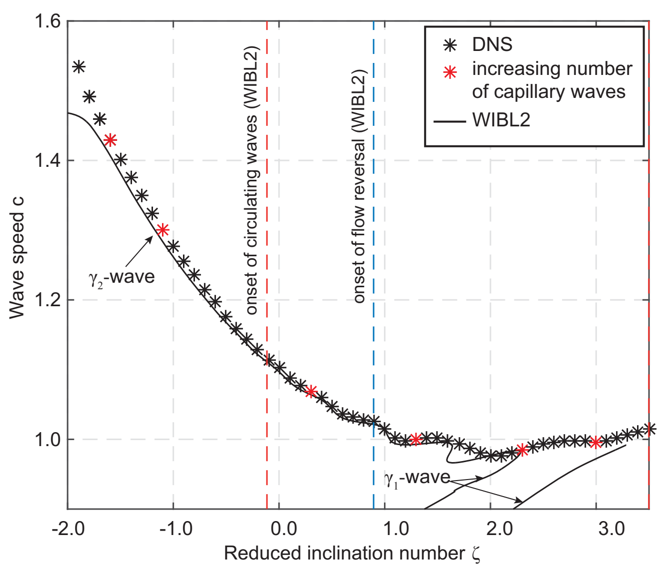

FIG. 7. Same as Fig. 6 but for the wave celerity.

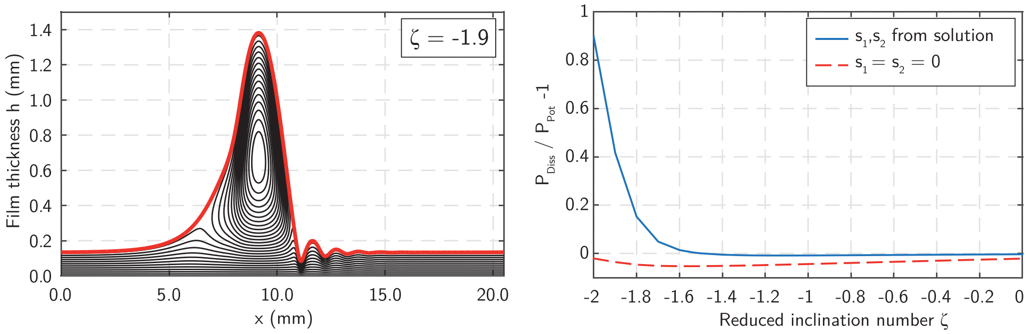

FIG. 8. Shown on the left are streamlines calculated with s_1 and s_2 set to zero for the inclined film flow of case 2 and $\zeta = [-1.9]$. Contour lines are shown for $\Delta\psi = 5 \times 10^{-6}$ m^2/s. Note that the thickness profile has been calculated with the WIBL2 model, i.e., including the s_1 and s_2 corrections. On the right is the ratio between viscous dissipation and the change in potential energy for case 2 and different values of the inclination number ζ.

to higher inclination numbers. With DNS, γ_2 waves were obtained for $\zeta \leqslant 3$ and γ_1 waves for $\zeta \geqslant 3.1$, using a sinusoidal wave with 25% amplitude for an initial condition.

The notation of γ_1 and γ_2 waves refers to the general shape of the wave, also referred to as family of waves [30]. The first family (γ_1 wave) is characterized by a dominant depression, a negative-hump solitary wave. Owing to a lower phase speed of those waves, this is the family of slow waves. The other family (γ_2 wave) is characterized by a dominant elevation, a positive-hump solitary wave. Due to the faster phase speed, this is the family of fast waves [1].

Both model approaches reveal in Figs. 6 and 7 a nonmonotonic variation of the wave celerity with the inclination number with small differences between $\zeta = 1.7$ and $\zeta = 1.9$. Such a nonmonotonic behavior was also found by Salamon *et al.* [31] for vertical film flows and a systematic variation in wave number. It was found that viscous dissipation in the streamwise direction influences this nonmonotonic behavior. Furthermore, viscous dissipation is known to affect significantly the number and amplitude of the capillary ripples preceding the main wave hump [1].

To verify whether the increasing number of capillary ripples is directly associated with the nonmonotonic variations seen in the wave celerity, profiles of the stationary traveling waves are compared in Fig. 10 for different values of ζ. In addition, the positions of local minima and maxima are indicated by blue and gray stars, respectively. Starting from the bottom profile with $\zeta = 3.5$,

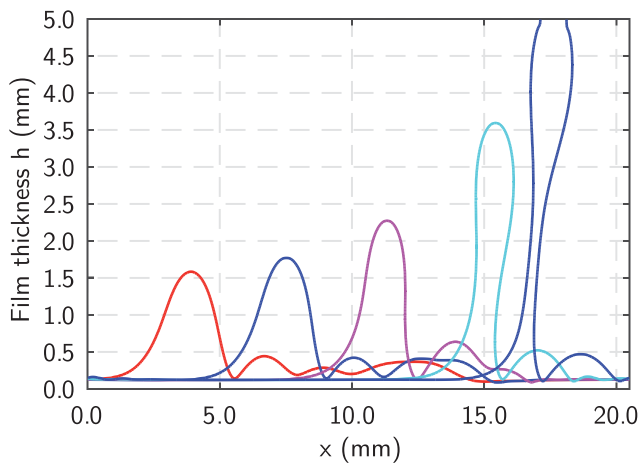

FIG. 9. Temporal evolution of dripping for an inclined film flow for case 2 and $\zeta = -2$.

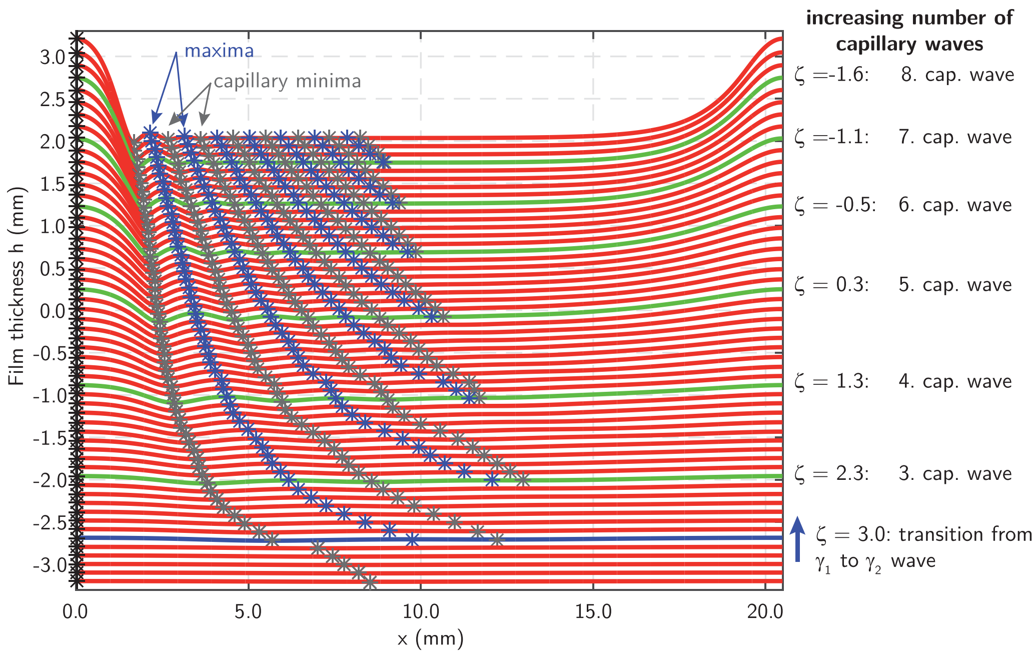

FIG. 10. Wave profile for $-1.9 \leqslant \zeta \leqslant 3.5$ by a skip of 0.1 with marked capillary maxima (blue) and minima (gray). All wave profiles are shifted to be visible. The increasing number of capillary waves indicated by the green wave profiles is shown for a decreasing value of ζ. The plot is based on direct numerical simulation results.

the inclination number decreases by 0.1 for each profile down to $\zeta = -1.9$. The first five profiles represent γ_1 waves with a very low amplitude. From $\zeta = 3.1$ to $\zeta = 3.0$ the wave type changes to γ_2 waves, which already exhibit a secondary maximum that moves closer to the main wave hump and turns into the maximum of the first capillary ripple if ζ is further decreased. Further minima and maxima arise for $\zeta = [2.3, 1.3, 0.3, -0.5, -1.1, -1.6]$ (green profiles) and the locations of all extrema move closer to the main wave hump with decreasing ζ values. In Fig. 7 the inclination numbers for which the number of capillary ripples increases by one are marked by red stars.

2. Case 1: Sinusoidal-like wave

The sinusoidal-like wave of case 1 is characterized by a high frequency, for which the wavelength (7.24 mm in the experiment) is not significantly larger than the capillary wavelength (in dimensional form $\lambda_c = \sqrt{\sigma/\rho g} = 2.11$ mm). Thus, a different behavior of the film flow is expected if the inclination number ζ is increased. Figure 11 shows a closer examination of the wave characteristics for inclination numbers of $\zeta = -2.5$, -3.0, and -3.5. Contrary to case 2, the wave profile is symmetric with a similar slope of the wave front and back. Only one capillary minimum in the wave front breaks the symmetry.

The two model approaches are in relatively good agreement for $\zeta = -2.5$. For $\zeta = -3$, the center of the circulating vortex moves closer to the back of the wave for WIBL2. The lateral shift of the vortex center is again prescribed by the corrections of s_1 and s_2. This behavior is not confirmed by the DNS. Differences in wave amplitude grow with decreasing inclination number, reaching approximately 10% for $\zeta = -3.5$.

Significant differences arise with the onset of dripping, as shown in Fig. 12. For these flow parameters ($\zeta = -4$), the WIBL2 model still predicts the existence of stationary traveling waves. In contrast, DNS predicts ligament detaching from the inclined ceiling. However, the exact value of

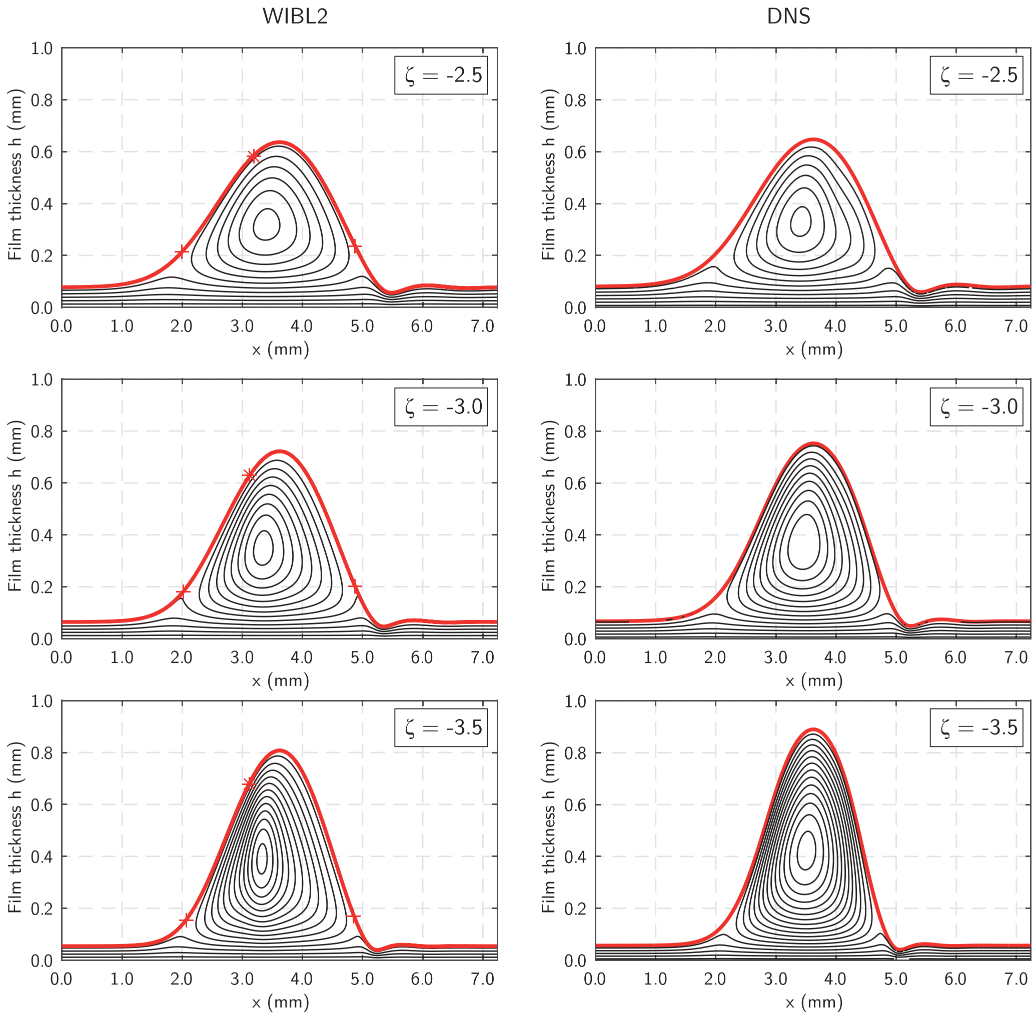

FIG. 11. Inclined film flow for case 1 and $\zeta = [-2.5, -3.0, -3.5]$. Contour lines are shown for $\psi = [2.5] \times 10^{-6}$ m^2/s. For WIBL2, streamlines have been calculated using the parabolic velocity profile with s_1 and s_2 as given by the model. Stars and crosses correspond to stagnation points and the location of maximal velocity, respectively.

droplet (or ligament) detachment is sensitive to the initial condition, so that dripping (as illustrated in Fig. 12) can also occur for lower inclination numbers if a favorable initial condition is used. Note that the onset of dripping strongly depends on the quality of the DNS code. Using the new interFoam solver allows one to explore stable waves for lower inclination numbers than using the standard interFoam solver.

Figure 13 shows the influence of stabilizing and destabilizing gravity by a variation of the reduced inclination number on wave amplitude and wave speed. Constant values for reduced Reynolds number, extensional viscous number, and wavelength are maintained. Results are obtained with the WIBL2 model (solid lines) and DNS (stars). The maximum film thicknesses resulting from the model and the fully resolved simulation are in good agreement for positive and negative values of the inclination number down to $\zeta = -2$. Decreasing the inclination number below this value, the WIBL2 predicts lower values of the maximum film thickness compared to the DNS. Note that no singularity, such as an infinite gradient of the film thickness (an orientation of the film surface

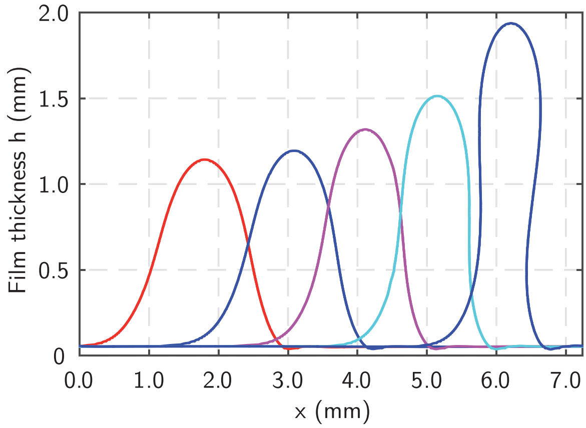

FIG. 12. Inclined film flow for case 1 and $\zeta = -4$.

perpendicular to the substrate), which could be associated with dripping, has been observed with the WIBL2 model. Instead, the WIBL2 model predicts a stationary traveling wave down to the lowest value of ζ explored, namely, $\zeta = -3.6$. This value coincides with the limit of the second-order dynamical system [see Eq. (4)]. The comparison of the wave celerity exhibits a lower degree of agreement, underestimating the phase speed as compared to DNS for $\zeta < -2$.

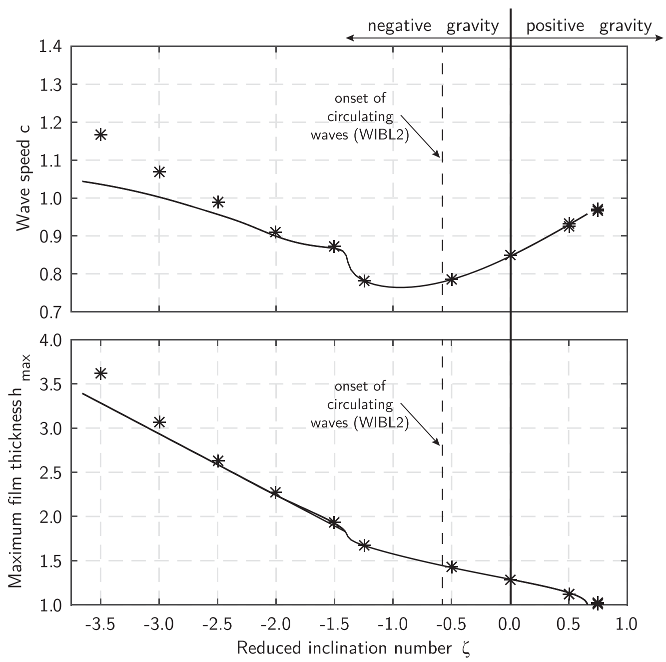

FIG. 13. Influence of stabilizing and destabilizing gravity on the maximum film thickness (top) and the wave celerity (bottom) by varying the inclination number ζ for the flow parameters corresponding to case 1. The stability limit (onset of waves) for this case is at $\zeta = 0.657$. The closed flow condition is applied for both the DNS (stars) and the WIBL2 model (solid line).

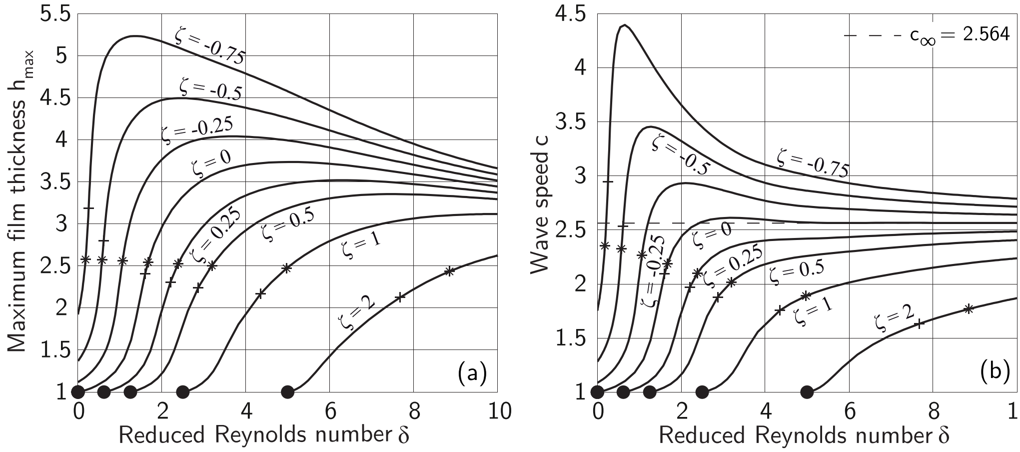

FIG. 14. Wave characteristics of negatively inclined falling films obtained with the WIBL2 model: (a) maximum film thickness and (b) wave celerity as a function of the reduced Reynolds number δ for $\eta = 0.1$. The stars indicate the onset of circulating waves, the crosses indicate the onset of flow reversal, and the closed circles indicate the onset of waves.

B. Waves characteristics in the homoclinic orbits

In the homoclinic orbit, a single wave pulse is considered in a sufficiently long spatial domain such that this wave pulse propagates on top of a substrate with a constant thickness h_s. Due to the single wave pulse, wavelength and frequency do not exist and the parameter space in the homoclinic orbit is reduced. Two important characteristics, i.e., maximum film thickness and wave celerity, are presented for stabilizing and destabilizing gravity conditions using the WIBL2 model (see Fig. 14). The simulation results are presented in Shkadov scaling and are limited to a single value of the extensional viscous number ($\eta = 0.1$). For the sake of comparison, results for a positive inclination number are replotted (see Fig. 2 in Ref. [16]). Values of the inclination number lower than $\zeta = -0.75$ are not shown for the sake of clarity. In addition, the limitation of the dynamical system of the WIBL2 model [see Eq. (4)] can also apply for negative values of the inclination number. For instance, solutions for an inclination number of $\zeta = -1.5$, together with a low value of the reduced Reynolds number ($\delta \approx 1$), cannot be obtained using the dynamical system (A7)–(A9).

The closed circles indicate the border of the stable flat film solution, e.g., $\delta < 5/2\zeta$, for $\zeta > 0$. For $\zeta \leqslant 0$ the film flow is always unstable such that the maximum film thickness starts to deviate from one for $\delta = 0$. An interesting effect of destabilizing gravity is found for very low values of the reduced Reynolds number (in the vicinity of $\delta = 0$). For these flow parameters, the wave is characterized by a nonzero amplitude and a phase speed above one. The amplitude and the phase speed increase with decreasing inclination number, indicating the formation of a very large amplitude and fast moving wave at relatively low but finite reduced Reynolds number. An increase of the reduced Reynolds number causes a steep increase in maximum film thickness and wave celerity crossing the onset of circulating waves and flow reversal. For the onset of circulating waves, a rather constant value of maximum film thickness is maintained for destabilizing gravity conditions. For the onset of flow reversal, the value of maximum film thickness increases with decreasing inclination number, eventually surpassing the critical value for the onset of circulating waves.

An important finding, especially for destabilizing gravity, is the decrease of the maximum film thickness with increasing the reduced Reynolds number beyond the maximum. This decreasing amplitude reveals a stabilization of the wave due the film flow. It can thus be expected that a film flow is able to prevent dripping for sufficiently large Reynolds numbers. Besides the maximum film thickness, also the wave speed decreases with increasing Reynolds number beyond the maximum (for higher negative values of the inclination number). According to Ruyer-Quil and Manneville

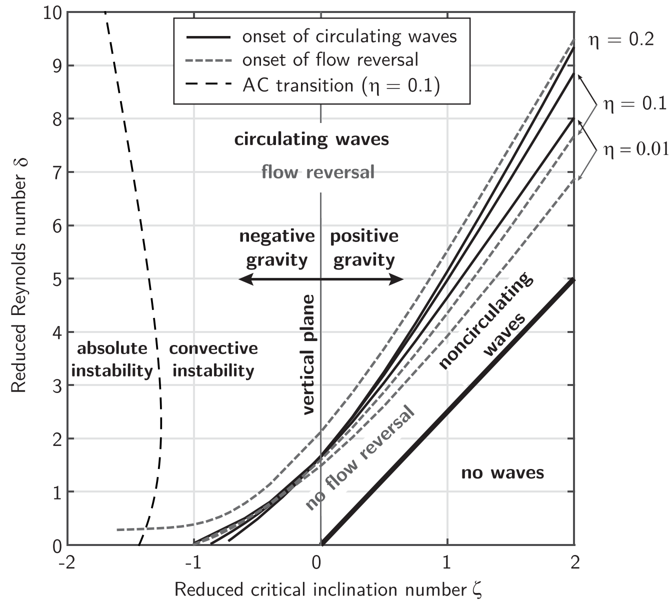

FIG. 15. Onset of flow reversal and circulating waves for homoclinic solutions and the absolute to convective instability transition, with a dependence on the dispersion number η, drawn by simulation results obtained from the WIBL2 model.

[32], the wave speed reaches a constant value of $c_\infty = 2.564$ as $\delta \to \infty$ using the WIBL2 model. Chakraborty *et al.* [33] confirmed this asymptotic value by DNS ($c_\infty = 2.560$). For negative values of the inclination number, this asymptotic value seems to exist as well. Note that for positive inclination numbers, the wave speed monotonically increases and approaches the asymptotic value from below. Contrarily, for larger negative values of the inclination number, the wave speed decreases beyond a maximum at low Reynolds numbers.

The phase diagram for waves in the homoclinic orbit presented in our previous study [16] is expanded to the regime of destabilizing gravity. The onset of circulating waves and flow reversal for one-hump homoclinic solutions (γ_2 waves) as a function of the reduced Reynolds number δ and the reduced inclination number ζ for various values of the streamwise extensional viscous number η is calculated based on the criteria given in Table I (see also Appendix B) and depicted in Fig. 15. The diagram shows the borders of three different transitions: onset of waves (thick black line), onset of circulating waves (black lines), and onset of flow reversal (gray dashed lines).

The diagram reveals that the onset of flow reversal is influenced more significantly by the extensional viscous number than the onset of circulating waves. In the destabilizing gravity domain, both transitions occur close to each other for $\eta = 0.01$ and $\eta = 0.1$. A different behavior is found for higher values of the extensional viscous number, i.e., $\eta = 0.2$. In this case, the onset of flow reversal appears to form a plateau for $\zeta < -1$ at a reduced Reynolds number above zero ($\delta \approx 0.25$). Thus, flow reversal occurs above a specific reduced Reynolds number only, independent from the inclination number, and also prior to flow recirculation.

The transition between absolute and convective instability is also plotted in this diagram for $\eta = 0.1$ following the steps given in Scheid *et al.* [15]. If the instability is of convective type, perturbations travel down the inclined plate while forming waves and eventually drops. If the instability is of absolute type, drops are formed at any location, causing droplet formation at the fluid inlet. The transition between absolute and convective instability is far beyond the onset of flow reversal and circulating waves and as we have shown in Figs. 9 and 12, convective dripping can occur corresponding to unsaturated waves in the convective instability region.

TABLE III. Correlations for the onset of circulating waves and flow reversal for positive and negative values of the inclination number (γ_2 waves). The dimensionless frequency f is defined as $f = \overline{f}\kappa t_\nu l_\nu / h_N$, where $\overline{f}$ is the dimensional frequency in Hz.

Onset of	Homoclinic orbit	Limit cycle
circulating waves	$\delta_{\text{circ}} \approx -1.28 + (2+\zeta)^{0.46\eta+1.6}$	$\delta_{\text{circ}} = -(2-29.5f) + (2+\zeta)^{1.75+21.5f}$
flow reversal	$\delta_{\text{rev}} \approx -1.28 + (2+\zeta)^{1.2\eta+1.5}$	omitted due to strong η dependence

C. Criteria for phase transitions in the limit cycle

Based on the simulation results in the homoclinic orbit (infinite wavelength and zero frequency) and limit cycle (finite wavelength and frequency), correlation equations for the critical reduced Reynolds number δ_{circ} and δ_{rev} can be deduced. The correlation equations, which are summarized in Table III, are derived from the WIBL2 simulation results and are valid in the stabilizing and destabilizing gravity regimes. The coefficients are very similar to the ones presented in our previous study for stabilizing gravity conditions.

In our previous study we had shown that a simplified criterion for phase transitions based on the ratio between maximum film thickness and the substrate film thickness is well suited to predict the onset of circulating waves. This ratio is found to remain rather constant despite any change of inclination, frequency, and extensional viscous number. In Fig. 16 the parameter space is extended to values of destabilizing gravity, as indicated by the large symbols. In addition, the threshold value for positive values of the inclination number are marked with small symbols (replotted from [16]). For the onset of flow reversal, the ratio between maximum and substrate film thickness indicated by the gray crosses is found to be dependent on reduced Reynolds and extensional viscous numbers. The ratio decreases with both parameters, but does not depend on frequency.

IV. CONCLUSION

In this study the hydrodynamics of two-dimensional waves in films flowing under an inclined plane was examined using fully resolved numerical simulations (DNSs) as well as the WIBL2 model.

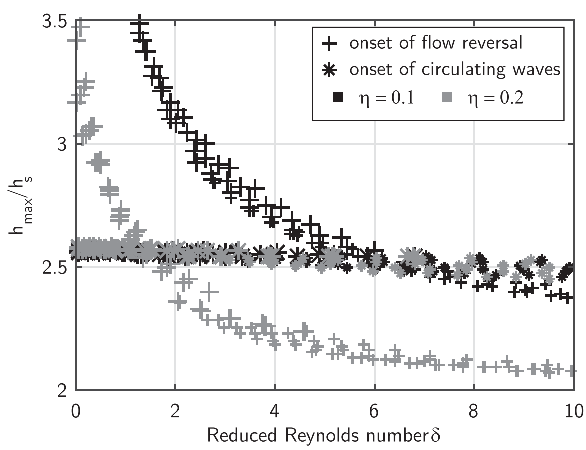

FIG. 16. Critical ratio between the maximum and substrate film thickness at the onsets of circulating waves and flow reversal. The symbols in the diagram represent results for different frequencies and inclination numbers. Black and gray symbols correspond to $\eta = 0.1$ and $\eta = 0.2$, respectively. The data are obtained by using the WIBL2 model. Data with positive inclination number are shown by the smaller symbols, while waves in the range of destabilizing gravity are shown by the larger symbols.

The DNS approach includes an interface compression scheme that reduces the amplitude of artificial velocities at the interface and allows for a precise prediction of falling films with high amplitudes. As a result, DNS and WIBL2 model results show excellent agreement in a wide range of inclination numbers. The two model approaches were also validated by comparison to experimental data of a vertical falling film showing very good agreement.

Under destabilizing gravity conditions, agreement between the WIBL2 model and the fully resolved numerical simulations is obtained prior to the onset of dripping. This includes the prediction of wave peak height and wave celerity. Differences in the velocity field predicted by the two model approaches are found for high-amplitude waves. It was shown that the WIBL2 results strongly violate the energy balance for stationary traveling waves, including viscous dissipation and the change in hydrostatic energy. Regarding the onset of dripping, the WIBL2 model is not suited for its prediction by nature as it is a single-value model.

In terms of wave characteristics, a nonzero amplitude and a dimensionless phase speed above one were identified for low values of the reduced Reynolds number (in the vicinity of $\delta = 0$), indicating the formation of a droplet riding on top of a very thin substrate. Increasing the reduced Reynolds number results in a decrease of maximum film thickness, revealing a stabilization of the wave due to the film flow and thus preventing dripping.

The phase diagram and the correlations for the onset of flow reversal and circulating waves presented in our previous study [16] were extended to the regime of destabilizing gravity. In addition, the simplified criteria for the two transitions based on the ratio between the maximum film thickness and the substrate film thickness were found to be valid in the destabilizing gravity regime as well. This ratio at the onset of circulating waves is rather constant irrespective of the inclination, frequency, and extensional viscous number. For the onset of flow reversal, this ratio decreases with reduced Reynolds number and depends on the extensional viscous number, but not on the forcing frequency. For low reduced Reynolds-number values, the ratio increases, showing an inverse proportionality.

A last critical comment should be given to the limitations of this study using a two-dimensional simulation domain only. Of course, the hanging film flow is subject to the Rayleigh-Taylor instability in the spanwise direction, leading to an early formation of a rivulet structure [34]. Waves riding on these rivulets will form droplets, leading to the detachment of single droplets. However, a detailed numerical investigation of three-dimensional falling films is computationally expensive. Thus, a validation of the numerical method (WIBL2 and DNS) and a detailed analysis of two-dimensional films is the first step in the analysis of hanging film flows.

ACKNOWLEDGMENT

B.S. thanks the F.R.S.-FNRS and BELSPO through MicroMAST Project No. IAP-7/38 for supporting this research.

APPENDIX A: FULL SECOND-ORDER WIBL2 MODEL

The four evolution equations for the (full second-order) WIBL2 model are

$$\partial_t h = \partial_x q, \tag{A1}$$

$$\begin{aligned}
\delta \partial_t q = {} & \frac{27}{28} h - \frac{81}{28} \frac{q}{h^2} - 33 \frac{s_1}{h^2} - \frac{3069}{28} \frac{s_2}{h^2} - \frac{27}{28} \zeta h \partial_x h + \frac{27}{28} h \partial_{xxx} h \\
& + \delta \left(- \frac{12}{5} \frac{q s_1 \partial_x h}{h^2} - \frac{126}{65} \frac{q s_2 \partial_x h}{h^2} + \frac{12}{5} \frac{s_1 \partial_x q}{h} + \frac{171}{65} \frac{s_2 \partial_x q}{h} + \frac{12}{5} \frac{q \partial_x s_1}{h} \right. \\
& \left. + \frac{1017}{455} \frac{q \partial_x s_2}{h} + \frac{6}{5} \frac{q^2 \partial_x q}{h^2} - \frac{12}{5} \frac{q \partial_x q}{h} \right)
\end{aligned}$$

$$+\eta\left(\frac{5025}{896}\frac{q(\partial_x h)^2}{h^2}-\frac{5055}{896}\frac{\partial_x q\partial_x h}{h}-\frac{10851}{1792}\frac{q\partial_{xx}h}{h}+\frac{2027}{448}\partial_{xx}q\right), \tag{A2}$$

$$\begin{aligned}\delta\partial_t s_1 =& \frac{1}{10}h-\frac{3}{10}\frac{q}{h^2}-\frac{126}{5}\frac{s_1}{h^2}-\frac{126}{5}\frac{s_2}{h^2}-\frac{1}{10}\zeta h\partial_x h+\frac{1}{10}h\partial_{xxx}h\\ &+\delta\left(-\frac{3}{35}\frac{q^2\partial_x h}{h^2}+\frac{1}{35}\frac{q\partial_x q}{h}+\frac{108}{55}\frac{qs_1\partial_x}{h^2}-\frac{5022}{5005}\frac{qs_2\partial_x h}{h^2}\right.\\ &\left.-\frac{103}{55}\frac{s_1\partial_x q}{h}+\frac{9657}{5005}\frac{s_2\partial_x q}{h}-\frac{39}{55}\frac{q\partial_x s_1}{h}+\frac{10557}{10010}\frac{q\partial_x s_2}{h}\right)\\ &+\eta\left(\frac{93}{40}\frac{q(\partial_x h)^2}{h^2}-\frac{69}{40}\frac{\partial_x q\partial_x h}{h}+\frac{21}{80}\frac{q\partial_{xx}h}{h}-\frac{9}{40}\partial_{xx}q\right),\end{aligned} \tag{A3}$$

$$\begin{aligned}\delta\partial_t s_2 =& \frac{13}{420}h-\frac{13}{140}\frac{q}{h^2}-\frac{39}{5}\frac{s_1}{h^2}-\frac{11817}{140}\frac{s_2}{h^2}-\frac{13}{420}\zeta h\partial_x h+\frac{13}{420}h\partial_{xxx}h\\ &+\delta\left(-\frac{4}{11}\frac{qs_1\partial_x h}{h^2}+\frac{18}{11}\frac{qs_2\partial_x h}{h}-\frac{2}{33}\frac{s_1\partial_x q}{h}-\frac{19}{11}\frac{s_2\partial_x q}{h}+\frac{6}{55}\frac{q\partial_x s_1}{h}-\frac{288}{385}\frac{q\partial_x s_2}{h}\right)\\ &+\eta\left(-\frac{3211}{4480}\frac{q(\partial_x h)^2}{h^2}+\frac{2613}{4480}\frac{\partial_x q\partial_x h}{h}-\frac{2847}{8960}\frac{q\partial_{xx}h}{h}+\frac{559}{2240}\partial_{xx}q\right).\end{aligned} \tag{A4}$$

For stationary periodic traveling waves moving with the wave celerity c, an integration of (A1) with $x' = x - c\,t$ gives a relation between the local flow rate $q(x')$ and the local film thickness $h(x')$:

$$q(x) = ch(x) + q_0, \tag{A5}$$

where the prime has been dropped for the sake of simplicity and q_0 denotes the rate at which the fluid moves under the wave, namely, backward in the moving frame of reference. Integrated over the wavelength λ, this equation gives a relation between the average flow rate and the average film thickness

$$\langle q\rangle_\lambda = c\langle h\rangle_\lambda + q_0. \tag{A6}$$

Fixing the flow rate, i.e., $\langle q\rangle_\lambda = 1/3$, corresponds to an open flow, while fixing the thickness, i.e., $\langle h\rangle_\lambda = 1$, corresponds to a closed flow condition.

The system of equations (A1)–(A4) can also be rewritten in the moving frame of reference for stationary periodic traveling waves. Replacing the time derivative of the flow rate $\partial_t q$ with $-c\partial_x q$ and all subsequent expressions of q with an expression of h according to (A5) results in the following third-order dynamical system (a system of ordinary differential equations):

$$\begin{aligned}h_{xxx} =& \{414720q_0^4\delta h_x + 216q_0^3[-13024+11\eta(2222h_x^2-1773hh_{xx})\\ &+640\delta h_x(14s_1+36s_2-11hc)] - 27456h^2c^2(196s_1+6771s_2)\\ &-132h^3c^3(-528+h_x[4525\eta h_x+576\delta(14s_1+9s_2)]\} + h^4c^3(37120\delta h_x c-99781\eta h_{xx})\\ &+3q_0hc\{-219\,648(133s_1+933s_2)+h^2c(73\,997\eta h_{xx}+34\,560\delta h_x c)\\ &+2hc[172\,128+h_x(-468\,479\eta h_x-786\,688\delta s_1+874\,752\delta s_2)]\}\\ &-72q_0^2\{247\,104(7s_1+32s_2)+hc[6424(4+9\eta h_x^2)\\ &-192\delta h_x(98s_1+1033s_2)c+hc(-26\,477\eta h_{xx}+8160\delta h_x c)]\}\\ &+2ch^3(11\,616ch^2+160\,507q_0h+468\,864q_0^2)(h_x\zeta-1)]/\\ &[2112h^3(-444q_0^2+152q_0hc+11h^2c^2)],\end{aligned} \tag{A7}$$

$$
\begin{aligned}
s_{1,x} = \big\{&8\,648\,640q_0(234s_1 + 779s_2) + 9q_0^2\big[1\,960\,192q_0\delta h_x \\
&- 143\eta\big(46\,458h_x^2 + 42\,233hh_{xx}\big) - 512\delta h_x(29\,617s_1 + 13\,887s_2)\big] \\
&+ 3hc[52q_0h_x(61\,504q_0\delta + 369\,391\eta h_x) + 3\,366\,935q_0\eta hh_{xx} \\
&+ 58\,240(803 + 450q_0\delta h_x)s_1 - 1920(-961\,961 + 32\,275q_0\delta h_x)s_2] \\
&+ 8h^2c^2\big[-12\,792q_0\delta h_x + 143\eta\big(16\,458h_x^2 + 3859hh_{xx}\big) \\
&+ 528\delta h_x(7483s_1 + 5058s_2)\big] - 1\,024\,192\delta h^3h_xc^3\big\}/ \\
&\big[147\,840\delta h\big(-444q_0^2 + 152q_0hc + 11h^2c^2\big)\big],
\end{aligned} \tag{A8}
$$

$$
\begin{aligned}
s_{2,x} = \big\{&808\,704q_0^3\delta h_x + 9q_0^2\big[143\eta\big(11\,566h_x^2 + 1291hh_{xx}\big) + 1536\delta h_x(273s_1 - 2147s_2 + 13hc)\big] \\
&+ 6q_0\big[29\,120s_1(759 + 34\delta hh_xc) + 1440s_2(167\,167 + 382\delta hh_xc) \\
&- 13hc\big(-3311\eta h_x^2 + 5170\eta hh_{xx} + 96\delta hh_xc\big)\big] + hc[-384\,384s_1(-20 + \delta hh_xc) \\
&- 6336s_2(8645 + 94\delta hh_xc)] + 13h^2c^2\big[-11\eta\big(3228h_x^2 + 919hh_{xx}\big) + 2048\delta hh_xc\big]\big\}\big/ \\
&\big[31\,680\delta h\big(-444q_0^2 + 152q_0hc + 11h^2c^2\big)\big],
\end{aligned} \tag{A9}
$$

where the subscript x indicates the x derivative.

APPENDIX B: CRITICAL WAVE CELERITY FOR THE ONSET OF CIRCULATING WAVES

The critical wave celerity at the onset of circulating waves and flow reversal was presented in our previous study [16]. However, as equality of the velocity at the wave crest with the wave celerity was assumed, no information was provided whether circulating waves exist above or below the obtained critical wave celerity. The following derivation clarifies this issue.

For the onset of circulating waves, the speed of the wave crest exceeds the wave celerity

$$u_{\max} > c. \tag{B1}$$

Introducing the parabolic profile (neglecting first-order corrections), using the relation for the local flow rate (A5), and assuming that the maximum fluid velocity is at the wave crest yields

$$\frac{3}{2}\left(c + \frac{q_0}{h_{\max}}\right) > c. \tag{B2}$$

For stationary periodic traveling waves, using (A6) to eliminate q_0, (B2) becomes

$$c + \frac{3\langle q\rangle_\lambda}{h_{\max}} - \frac{3c\langle h\rangle_\lambda}{h_{\max}} > 0. \tag{B3}$$

Rearranging the equation leads to

$$c(h_{\max} - 3\langle h\rangle_\lambda) > -3\langle q\rangle_\lambda \tag{B4}$$

and the multiplication of the equation by -1 yields

$$c(3\langle h\rangle_\lambda - h_{\max}) < 3\langle q\rangle_\lambda. \tag{B5}$$

Isolating the wave celerity, we finally obtain

$$c < \frac{3\langle q\rangle_\lambda}{3\langle h\rangle_\lambda - h_{\max}} \equiv c_{\text{circ}}. \tag{B6}$$

The equation above states that the wave celerity above the onset of circulating waves should be lower than the critical wave celerity.

Note that $3\langle h\rangle_\lambda - h_{\max}$ is always positive at the onset of recirculating waves since $h_{\max}/h_s$ is smaller than 3 (see Fig. 15) and $\langle h\rangle_\lambda$ is always larger than h_s such that $h_{\max}/\langle h\rangle_\lambda < h_{\max}/h_s$. It is thus also required that the condition $h_{\max}/h_s < 3$ is fulfilled, which appears together with the criterion for the onset of circulating waves. Considering a flat film for which the celerity of infinitesimal wave perturbation is $c = 1$, the inequality equation for the onset of circulating waves requires

$$c < \frac{3 \times 1/3}{3 \times 1 - 1} = \frac{1}{2} \equiv c_{\text{circ}}, \tag{B7}$$

which is obviously not verified, indicating that there are obviously no circulating waves for small-amplitude waves.

APPENDIX C: RECONSTRUCTION METHODS FOR THE VELOCITY FIELD

The velocity field for the WIBL2 model is calculated by evaluating the streamwise and cross-stream velocities (for details see, e.g., [1]). The streamwise velocity, including the first-order corrections (s_1 and s_2 directly obtained from the model results) to the parabolic velocity profile, is given by

$$\begin{aligned} u(x,y) = {} & \frac{3}{h}(q - s_1 - s_2)\left(\bar{y} - \frac{1}{2}\bar{y}^2\right) + 45\frac{s_1}{h}\left(\bar{y} - \frac{17}{6}\bar{y}^2 + \frac{7}{3}\bar{y}^3 - \frac{7}{12}\bar{y}^4\right) \\ & + 210\frac{s_2}{h}\left(\bar{y} - \frac{13}{2}\bar{y}^2 + \frac{57}{4}\bar{y}^3 - \frac{111}{8}\bar{y}^4 + \frac{99}{16}\bar{y}^5 - \frac{33}{32}\bar{y}^6\right), \end{aligned} \tag{C1}$$

where $\bar{y} = y/h(x)$. The cross-stream velocity is straightforwardly calculated based on

$$v(x,y) = -\int_0^y \frac{\partial[u(x,Y)]}{\partial x}dY. \tag{C2}$$

APPENDIX D: ENERGY BALANCE IN STATIONARY TRAVELING WAVES

The energy balance in stationary traveling waves includes the change in hydrostatic potential energy (acting as a source of energy while the wave is traveling downstream), which is balanced by viscous dissipation. Other energies, such as kinetic energy or surface tension-driven energy, remain constant.

In general, the viscous dissipation rate in a two-dimensional domain is given by

$$\Phi = 2\nu\left[\left(\frac{\partial u}{\partial x}\right)^2 + \left(\frac{\partial v}{\partial y}\right)^2 + \frac{1}{2}\left(\frac{\partial u}{\partial y} + \frac{\partial v}{\partial x}\right)^2\right], \tag{D1}$$

where Φ is given in units of $\mathrm{m}^2/\mathrm{s}^3$. The integral of the dissipation rate is

$$P_{\text{diss}} = \int \rho\Phi\, dV \tag{D2}$$

and the integral of the change in hydrostatic potential energy is given by

$$P_{\text{pot}} = \int \rho u g_x dV. \tag{D3}$$

If the velocity field is given in Shkadov scaling, the two energies are given by

$$P_{\text{diss}} = \rho\frac{\bar{h}_N^5 g_x^2}{\nu}\int\left[\left(\frac{\partial u}{\kappa\partial x}\right)^2 + \left(\frac{\partial v}{\kappa\partial y}\right)^2 + \frac{1}{2}\left(\frac{\partial u}{\partial y} + \frac{\partial v}{\kappa^2\partial x}\right)\right]\kappa^2 dV \tag{D4}$$

and

$$P_{\mathrm{pot}} = \rho \frac{\bar{h}_N^5 g_x^2}{\nu} \int u\kappa^2 dV. \tag{D5}$$

[1] S. Kalliadasis, C. Ruyer-Quil, B. Scheid, and M. G. Velarde, *Falling Liquid Films* (Springer, London, 2013).

[2] A. Oron and P. Rosenau, Formation of patterns induced by thermocapillarity and gravity, J. Phys. (France) II **2**, 131 (1992).

[3] F. F. Abdelall, S. I. Abdel-Khalik, D. L. Sadowski, S. Shin, and M. Yoda, On the Rayleigh-Taylor instability for confined liquid films with injection through the bounding surfaces, Int. J. Heat Mass Transfer **49**, 1529 (2006).

[4] L. Rayleigh, Investigation of the character of the equilibrium of an incompressible heavy fluid of variable density, Proc. London Math. Soc. **14**, 170 (1883).

[5] S. Chandrasekhar, *Hydrodynamics and Hydromagnetic Stability* (Oxford University Press, Oxford, 1961).

[6] M. Fermigier, L. Limat, J. E. Wesfreid, P. Boudinet, and C. Quilliet, Two-dimensional patterns in Rayleigh-Taylor instability of a thin layer, J. Fluid Mech. **236**, 349 (1992).

[7] A. D. Myshkis, V. G. Babskii, N. D. Kopachevskii, L. A. Slobozhanin, and A. D. Tyuptsov, *Low-Gravity Fluid Mechanics—Mathematical Theory of Capillary Phenomena* (Springer, Berlin, 1987).

[8] G. H. Wolf, Dynamic Stabilization of Interchange Instability of a Liquid-Gas Interface, Phys. Rev. Lett. **24**, 444 (1970).

[9] N. A. Bezdenezhnykh, V. A. Briskman, A. A. Cherepanov, and M. T. Sharov, Control of the stability of liquid surfaces by means of variable fields, Fluid Mech. Sov. Res. **15**, 11 (1986).

[10] B. K. Kopbosynov and V. V. Pukhnachev, Thermocapillary flow in thin liquid films, Fluid Mech. Sov. Res. **15**, 95 (1986).

[11] R. J. Deissler and A. Oron, Stable Localized Patterns in thin Liquid Films, Phys. Rev. Lett. **68**, 2948 (1992).

[12] P. H. Trinh, H. Kim, N. Hammoud, P. D. Howell, S. J. Chapman, and H. A. Stone, Curvature suppresses the Rayleigh-Taylor instability, Phys. Fluids **26**, 051704 (2014).

[13] A. J. Babchin, A. L. Frenkel, B. G. Levich, and G. I. Sivashinsky, Nonlinear saturation of Rayleigh-Taylor instability in thin films, Phys. Fluids **26**, 3159 (1983).

[14] P.-T. Brun, A. Damiano, P. Rieu, G. Balestra, and F. Gallaire, Rayleigh-Taylor instability under an inclined plane, Phys. Fluids **27**, 084107 (2015).

[15] B. Scheid, N. Kofman, and W. Rohlfs, Critial inclination for absolute/convective instability transition in inverted falling films, Phys. Fluids **28**, 044107 (2016).

[16] W. Rohlfs and B. Scheid, Phase diagram for the onset of circulating waves and flow reversal in inclined falling films, J. Fluid Mech. **763**, 322 (2015).

[17] D. Reck and N. Aksel, Recirculation areas underneath solitary waves on gravity-driven film flows, Phys. Fluids **27**, 112107 (2015).

[18] H. Jasak, Error analysis and estimation for the finite volume method with applications to fluid flows, Ph.D. thesis, Imperial College, University of London, 1996.

[19] O. Ubbink, Numerical prediction of two fluid systems with sharp interfaces, Ph.D. thesis, Imperial College, University of London, 1997.

[20] H. Rusche, Computational fluid dynamics of dispersed two-phase flows at high phase fractions, Ph.D. thesis, Imperial College, University of London, 2002.

[21] C. W. Hirt and B. D. Nichols, Volume of fluid (VOF) method for the dynamics of free boundaries, J. Comput. Phys. **39**, 201 (1981).

[22] J. U. Brackbill, D. B. Kothe, and C. Zemach, A continuum method for modeling surface tension, J. Comput. Phys. **100**, 335 (1992).

[23] S. S. Deshpande, L. Anumolu, and M. F. Trujillo, Evaluating the performance of the two-phase flow solver interFoam, Comput. Sci. Disc. **5**, 014016 (2012).

[24] B. Lafaurie, C. Nardone, R. Scardovelli, S. Zaleski, and G. Zanetti, Modelling merging and fragmentation in multiphase flows with SURFER, J. Comput. Phys. **113**, 134 (1994).

[25] P. Pischke and W. Rohlfs (unpublished).

[26] C. Ruyer-Quil and P. Manneville, Improved modeling of flows down inclined planes, Eur. Phys. J. B **15**, 357 (2000).

[27] E. J. Doedel, AUTO-07P: *Continuation and bifurcation software for ordinary differential equations* (Concordia University, Montreal, 2008).

[28] G. F. Dietze, F. Al-Sibai, and R. Kneer, Experimental study of flow separation in laminar falling liquid films, J. Fluid Mech. **637**, 73 (2009).

[29] G. F. Dietze, Flow separation in falling liquid films, Ph.D. thesis, RWTH Aachen, 2010.

[30] H.-C. Chang, E. A. Demekhin, and D. I. Kopelevich, Construction of stationary waves on a falling film, Comput. Mech. **11**, 313 (1993).

[31] T. R. Salamon, R. C. Armstrong, and R. A. Brown, Traveling waves on vertical films: Numerical analysis using the finite element method, Phys. Fluids **6**, 2202 (1994).

[32] C. Ruyer-Quil and P. Manneville, On the speed of solitary waves running down a vertical wall, J. Fluid Mech. **531**, 181 (2005).

[33] S. Chakraborty, P.-K. Nguyen, C. Ruyer-Quil, and V. Bontozoglou, Extreme solitary waves on falling liquid films, J. Fluid Mech. **745**, 564 (2014).

[34] B. Scheid, Rivulet structures in falling liquid films, in *Without Bounds: A Scientific Canvas of Nonlinearity and Complex Dynamics*, Understanding Complex Systems, 1st ed., edited by R. G. Rubio, Yu. S. Ryazantsev, V. M. Starov, G.-X. Huang, A. P. Chetverikov, P. Arena, A. A. Nepomnyashchy, A. Ferrús and E. G. Morozov (Springer-Verlag, Berlin, Heidelberg, 2013).